ORIGINAL ARTICLE

lajss.org© Latin American Journal of Solids and Structures

www.lajss.org

Experimental and Numerical Study on Ballistic Impact Response of Vehicle Tires

Yangziyi Ji[a], Xiangdong Li[a]*, Lanwei Zhou[a], Xingfeng Liu[b]

[a]Nanjing University of Science and Technology; Nanjing, 210094, China. Email: jyzynjust@njust.edu.cn, lixiangd@njust.edu.cn, lwzhou@njust.edu.cn

[b]Chongqing Hongyu Precision Industrial Co. Ltd, Chongqing 402760, China. Email: liuxingfeng2009@qq.com

* Corresponding author

https://doi.org/10.1590/1679-78257764

Abstract

Tires are a critical component of military wheeled vehicles and are exposed to the threat of fragment caused by explosion of warhead on the battlefield. To study the ballistic impact response of military vehicle tires under fragment, experiments and numerical simulations of spherical fragments impacting tires were carried out. The damage mode of the tires was analyzed. The effects of obliquity, tire thickness, and fragment mass on the dynamic response of tires, as well as the ballistic limit velocity, were analyzed. The results indicate that: (1) The main failure modes of the tire comprise local erosion near the center of the perforation, elastic deformation surrounding the perforation, and tensile fracture of the steel cords. (2) The process of fragment penetration into a tire can be divided into four stages: the entry stage, stable penetration stage, cord layer penetration stage, and fragment exit stage. (3) The cord structure demonstrates its ability to undergo plastic deformation to a certain extent and its restraining effect on the rubber.

Keywords

tire; fragment, penetration, numerical simulation, failure mode.

Graphical Abstract

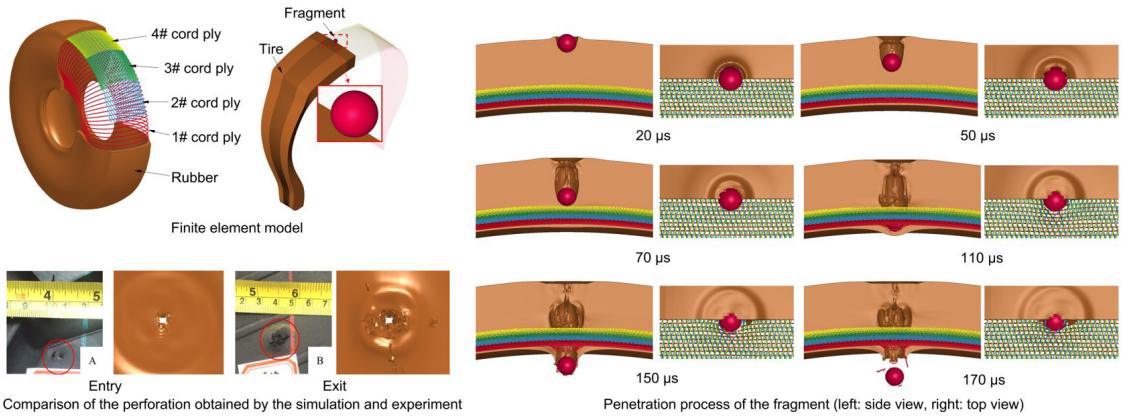

Comparison of the perforation obtained by the simulation and experiment

Penetration process of the fragment (left: side view, right: top view)

Received: July 12, 2023. In revised form: July 17, 2023. Accepted: July 17, 2023. Available online: July 21, 2023
https://doi.org/10.1590/1679-78257764

1 INTRODUCTION

Military vehicles are critical components of modern weapon systems, with wheeled vehicles accounting for approximately 75% of such equipment. This category includes a diverse range of vehicles, such as transport vehicles, command vehicles, tractors, communication vehicles, and missile launch vehicles. Tires are essential parts of wheeled vehicles as they are in direct contact with the ground and bear the weight of the entire vehicle. On the battlefield, military vehicles are susceptible to damage from the shock wave generated by ammunition explosions and the penetration of high-velocity fragments. This can significantly reduce the mobility of the vehicle and hinder its effectiveness in completing its mission. Thus, it is crucial to conduct research on the damage caused to tires to analyze the vulnerability of military vehicles.

Concerning the tire damage caused by shock wave, Baranowski et al.(Baranowski, Malachowski, & Mazurkiewicz, 2016b; Baranowski, Malachowski, Janiszewski, et al., 2016a; Baranowski et al., 2019) developed a detailed finite element model of truck tires, measuring the mechanical properties of rubber materials using a uniaxial testing machine and Hopkinson compression bars to implement a simplified rubber intrinsic model available in the LS-DYNA code. Blast load tests were also conducted for different distances to study the interaction of the tire with the local blast wave. By optimizing the cord angle and structure, the local damage of the tire was reduced, and the blast resistance of the tire was improved. Compared with the explosion shock wave, high-velocity fragments possess good energy storage properties and can penetrate military vehicle tires. Grote et al. (Grote et al., 1995) conducted vulnerability analyses of wheeled vehicles under attack from small steel and tungsten fragments weighing less than 0.65 g. Danish (Danish, 1968, 1973) developed penetration equations from experimental data involving steel right circular cylinder fragment simulators weighing from 0.32 to 7.78 g fired against various tire thicknesses, but the results are not publicly available.

Tires are considered a typical flexible composite material due to their composition of cords and rubber matrix, where each material has unique mechanical properties. Rubber is a high-polymer material known for its elasticity and energy absorption properties. It can stretch several times its original length when loaded and returning almost to its original size after unloading. Rubber also exhibits high damping characteristics and shock resistance, making it suitable for use as a protective layer under shock loads (Khodadadi et al., 2021). Studies have been also conducted to investigate the ballistic performance of rubber materials. Khodadadi et al. (Khodadadi et al., 2019) tested two types of rubber panels with different compound ingredients, subjected them to high-velocity impact tests, and found that the damage zone increased as the diameter of the projectile increased. Hong et al. (Hong et al., 2021) conducted an experiment using a spherical fragment to penetrate a natural rubber plate and found that damage caused by plastic penetration and tensile failure was greater than that caused by shear failure. Ishikawa et al. (Ishikawa et al., 2005) conducted a study on the effect of hybrid gel-rubber materials, temperature, and bullet type on the depth of rubber required to stop a bullet. The results of the study showed that cold temperature makes rubber materials harder and stronger, which in turn causes the rubber depth required to stop a bullet at cold temperatures to be smaller than that required at hot temperatures. Molnar et al. (Molnar et al., 2015) employed a gas gun to propel 9 mm spherical steel balls towards the surface of a rubber conveyor belt, maintaining a constant velocity of 37 m/s. They measured maximum penetration depths of up to 3.9 mm, along with maximum dissipated energies reaching 86.8%. Cai et al. (Cai et al., 2015, 2016) studied the ballistic resistance and self-sealing behavior of hydrogenated nitrile butadiene rubber (HNBR) enhanced with polyhedral oligomeric silsesquioxane (POSS) subjected to high speed impact experimentally and numerically. The results indicate that the coating layer can increase the ballistic limit of TC-128 steel plates.

In summary, there is a relatively limited amount of research in the open literature regarding the penetration of fragments into tires, and there has not been an analysis of the dynamic response process of tire structures under the influence of fragment impact. In this study, both experimental and numerical investigations were conducted on a typical truck tire subjected to impacts from spherical fragments. The explicit finite element code LS-DYNA was utilized to model

the fragment impact on the tire, and experimental validation was carried out to ensure the accuracy of the results. Using the validated model, several critical factors affecting the ballistic limit of the fragment on the tire were examined, including obliquity, tire thickness, and fragment mass.

2 TIRE CHARACTERISTICS AND MODELLING

2.1 Tire characteristics

This study utilized a 16.00R20 model radial tire with an outer diameter of 1320 mm. The tire's basic characteristics are presented in Table 1, while its cross-sectional structure is shown in **Figure 1**. The tire is comprised of six primary components, namely the crown, sidewall, belt layer, carcass, bead, and inner liner (also known as the airtight layer). The carcass cords of radial tires are positioned in the same direction as the Earth's meridian, with the axle serving as the center, extending from one bead to another. While the belt cords are also positioned obliquely and crosswise, they form a slight angle (usually ranging from 15° to 25°) with the centerline of the crown. The cord layers, ranging from inside to outside, are 1 # cord layer, 2 # cord layer, 3 # cord layer, and 4 # cord layer. The thickness of the inner liner measures 3.5 mm, while most of the sidewall has a thickness of 14.7 mm. The remaining part's thickness gradually increases towards both sides. The tire crown's thickness is 39.5 mm, and the pattern's convex and concave parts measure 19.5 mm and 27.5 mm, respectively. The cord layer is comprised of steel cords and base rubber, while the remainder of the structure consists of rubber.

Table 1 Tire parameters (16.00R20)

Tire type	Outer diameter d/mm	Diameter of the wheel rim/in	section width/mm	Circumference/mm
16.00R20	1320	10	438	4147

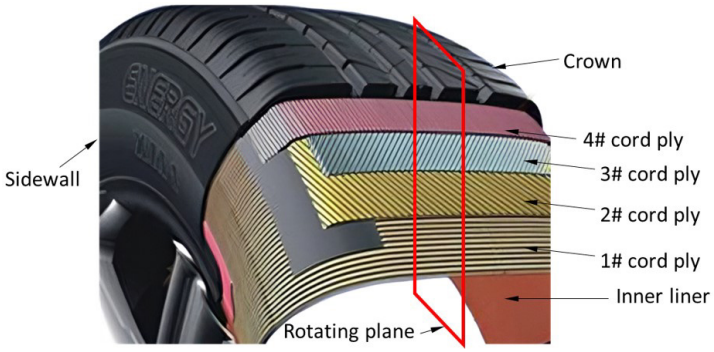

Figure 1 Schematic diagram of tire structure.

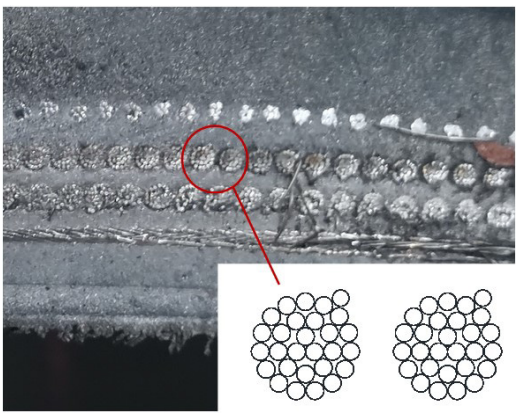

Figure 2 The structure of the tire cord (3+9+15×0.22+0.15).

The structure and parameters of the cord are illustrated in **Figure 2** and described in **Table 2**, respectively. In the table, the angle between the cord and the rotation plane (as shown in **Figure 1**) is denoted by α, with the counterclockwise direction considered positive. The structure of a single cord is represented by the notation 3+9+15×0.22+0.15, which indicates that the cord is composed of three strands of 0.22 mm diameter, nine strands of 0.22 mm diameter, fifteen strands of 0.22 mm diameter, and a final strand of 0.15 mm diameter (as shown in **Figure 2**).

Table 2 Cord Structure Parameters.

Cord layer	Single cord structure/mm	Laminating material	Thickness/mm	α/°
1#	3+9+15×0.22	ALT	3.2	90
2#	3+9+15×0.22+0.15	ABS	2.4	24
3#	3+9+15×0.22+0.15	ABS	2.4	-15
4#	5×0.35	ABS	1.6	15

2.2 Tire modelling

Due to the fact that the two-dimensional profile of the tire is mostly composed of circular arcs and is covered by ABS material, the three-dimensional modeling of the tire is difficult. To establish a three-dimensional model of the tire, the following method was used: the two-dimensional cross-sectional diagram of the tire was drawn in AutoCAD and a Sat format file was generated. This file was imported into ANSYS, and the cross-section was used to generate a three-dimensional solid using ANSYS. As stated in section 2.1, the tire is a layered structure, therefore the tire was divided into seven parts from the inside out for modeling, as shown in **Figure 3**, these seven parts are: (1) the first layer basic structure with the inner liner as the base; (2) the second layer composed of cord fabric and rubber; (3) the third layer composed of cord 1# and rubber; (4) the fourth layer composed of cord 2# and rubber; (5) the fifth layer composed of cord 3# and rubber; (6) the sixth layer composed of sidewalls and crown; and (7) the remaining structure. Using the rotational extrusion function in ANSYS, the three-dimensional model of the tire was obtained based on the above method.

The cord is the reinforcing material of the tire, that is, the skeleton material. It is composed of multiple steel wires that are arranged and bonded in a specific pattern. Therefore, to accurately model the tire, the number of wires in each cord layer must be considered. Structural parameters such as the cross-sectional area, spacing, and laying angle of each steel cord are defined to simulate the precise position of the cord within the rubber material. The location of each cord layer within the tire has been determined using the cross-sectional view provided in section 2.1. The cord is generated by extracting the line body that stretches to form the mid-surface of the cord layer and performing various operations such as arrays. The established three-dimensional model of the tire is shown in **Figure 4**.

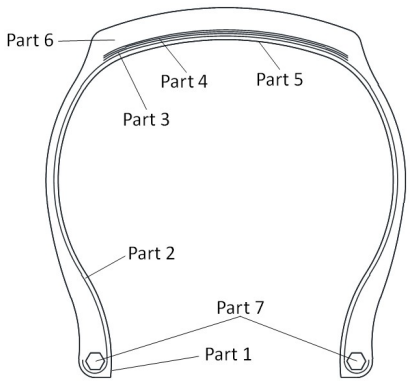

Figure 3 Schematic diagram of layers and modules of tires.

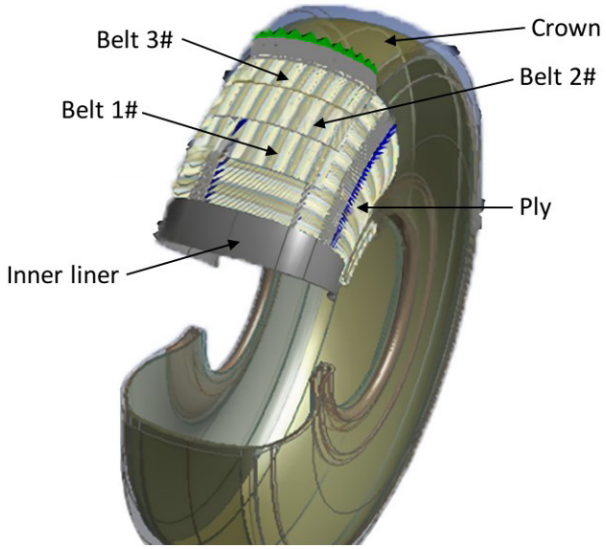

Figure 4 Model of the tire.

3 IMPACT EXPERIMENT AND SIMULATION MODEL

3.1 Experimental setup

To analyze the damage mode of the tire under the impact of fragments, penetration tests were conducted on the tire using a ballistic gun. The experimental setup is shown in **Figure 5**. The fragments used were a tungsten sphere with diameter 11 mm and a mass of 12.5 g. To capture the entire process of impact, a high-speed video camera (Phantom V641) was employed, with a frame rate of 7000 per second. The impact and residual velocities of the fragment were measured using high-speed framing photographic techniques, and make/break screens were used as a backup plan.

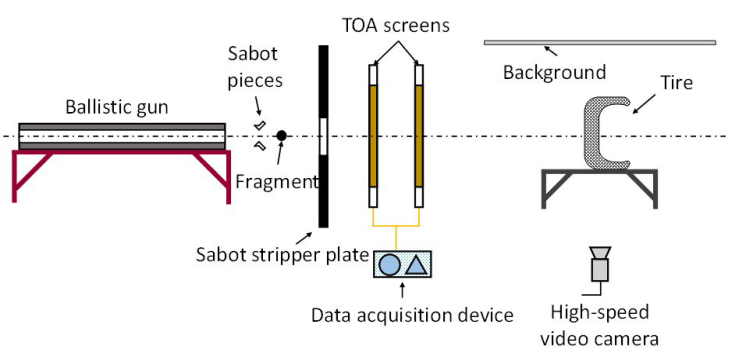

(a) Schematic.

(b) Actual apparatus.

Figure 5 The experimental setup.

Due to the large overall dimensions of the tire and the annular structure of the tire, which is inconvenient for installation and fixation during the experiment, the tire was cut into ten equal pieces, as depicted in **Figure 6**. The cutting parameters used are presented in Table 3. The resulting section structure of the tire after cutting is shown in **Figure 7**.

Table 3 Experiment tire cutting parameters.

d/mm	Cut segments	length/mm	ϑ/°	L_1/mm	L_2/mm
1320	10	414.7	36	407.9	517.0

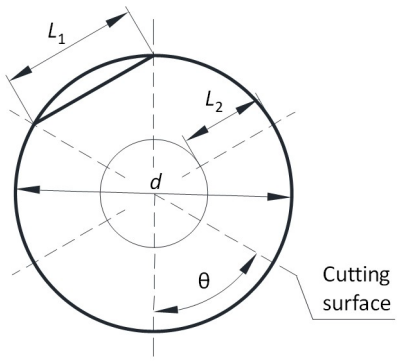

Figure 6 Schematic diagram of tire cutting size.

Figure 7 sectional structure of the tire after cutting.

3.2 Simulation model

3.2.1 Simplification of the cord

As depicted in **Figure 2**, a single cord is composed of multiple thin steel wires twisted at a specific pitch and direction. For simplification, a single cord is treated as a single steel wire with the same cross-sectional area.

$$d = \sqrt{\sum_{i=1}^{n} d_i^2} \tag{1}$$

where d_i is the diameter of the i-th thin steel wire in a single cord; n is the number of thin steel wires in a single cord; d is the equivalent diameter of a single cord.

3.2.2 Mesh of the model

ANSYS/LS-DYNA was used to conduct numerical simulation of fragment penetrating the tire. Meshing is an important aspect of finite element simulation, and the shape, size, and arrangement of the mesh directly affect the accuracy of the simulation results, the time required for simulation, and the smoothness of the simulation process. Due to the complex shape of the tire, the following principles are followed when meshing: the density of the mesh in the transition regions between adjacent areas is similar, and the lengths of the elements' sides are made as equal as possible.

Considering the regularity of the model, the tire model is divided into the crown and sidewall, and meshing is performed separately for each. Solid elements are used to build the mesh model for the crown part, with a denser

mesh in the area where the tire contacts with fragment and a coarser mesh in the rest, resulting in the mesh model for the crown as shown in **Figure 8**(a). The same meshing method was applied to the sidewall, but due to its more complex shape compared to the crown, it was challenging to control the shape of the mesh in certain areas. Therefore, irregularly shaped regions were designated as non-contact areas between the fragment and the sidewall, resulting in the mesh model for the sidewall as shown in **Figure 8**(b).

(a) Crown. (b) Sidewall.

Figure 8 Mesh of the crown and sidewall.

A beam element is used to build the model for the cord structure, with each mesh having a length of 0.5mm. The meshed cord structure is shown in **Figure 9**.

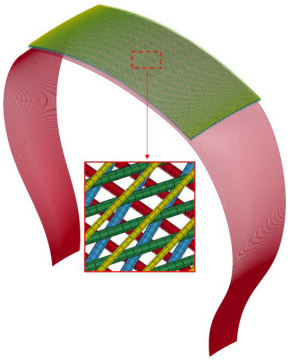

Figure 9 Mesh of cords.

The established finite element model of tire is shown in **Figure 10**(a). Since the damage to the tire caused by the fragment penetration is concentrated in a localized area of the impact region, in order to reduce the computational time. Following a similar approach to the experimental treatment of the tire, a finite element model was established as shown in **Figure 10**(b) for subsequent analysis and calculations. The penalty-based eroding surface-to-surface contact algorithm was employed to simulate the interaction between the fragment and tire. Additionally, the automatic surface-to-surface contact algorithm was employed to model the interaction between the cord fabric and the rubber material. The *CONSTRAINED_LAGRANGE_IN_SOLID keyword was utilized to simulate the interaction between the cord fabric and the rubber material.

(a) Mode of tire. (b) Model of fragment penetrates tire.

Figure 10 Finite element model.

3.2.3 Material model and parameters

The Mooney-Rivlin model is used to describe dynamic response the rubber material, which can simulate the strain energy of incompressible isotropic hyperelastic materials. The strain energy density function *W* is defined as (Hall et al., 2004; Hallquist, 2007):

$$W = A(I_1 - 3) + B(I_2 - 3) + C\left(I_3^{-2} - 1\right) + D(I_3 - 1)^2 \tag{2}$$

where: $C = 0.5A + B$, $D = \left[A(5\mu - 2) + B(11\mu - 5)\right] / \left[2(1 - 2v)\right]$, μ is the poisson's ratio, $2(A + B)$ is the shear modulus of linear elasticity, I_1, I_2, I_3 are the invariants of right Cauchy-Green Tensor C. The erosion failure of the Mooney-Rivlin model was added, the maximum failure principal strain was set to 1 and the maximum failure principal stress was set to 180 MPa. The material fails when both failure conditions are reached.

The materials of fragment and cord are described by the Plastic-Kinematic model, which considers the strain rate effect of the material. The yield strength of the material under dynamic loading is

$$\frac{\sigma_{\mathrm{Sd}}}{\sigma_{\mathrm{Sj}}} = 1 + \left(\frac{\dot{\varepsilon}}{C}\right)^{1/P} \tag{3}$$

where *P* and *C* are the material parameters; $\dot{\varepsilon}$ is the strain rate; σ_{sd} is the dynamic yield strength; σ_{sd} is the static yield strength.

The material parameters used in the simulation are shown in **Table 4** (Sun & Chen, 2021; Zhang et al., 2020), where ρ is the material density; E is the elastic modulus; F_s is the failure strain; E_t is the tangent modulus.

Table 4 Material parameters.

Material	ρ/(kg·m^{-3})	E/GPa	μ	F_s	σ_{sj}/MPa	P	C	E_t/MPa	A/MPa	B/MPa
rubber	1850	-	0.495	-	-	-	-	-	5.54	0.9853
Tungsten	18000	350	0.3	0.6	930	-	-	2160	-	-
steel	7830	210	0.3	0.03	1150	4.04×10^{-4}	5	1860	-	-

3.3 Simulation validation

3.3.1 Fragment residual velocity

Table 5 and **Figure 11** provide a comparison between the fragment residual velocities v_r obtained from the experiments and simulations at different impact velocities v_i. In **Figure 11**, the lines through the data points are fitted based on the R-I model (Recht & Ipson, 1963):

$$v_r = a\left(v_i^p - v_c^p\right)^{1/p} \tag{4}$$

where the method of least squares was used to obtain a best fit of the model constants *a* and *p* to the data.

As the results show, the maximum relative error of the fragment residual velocity calculated by simulation is 11.42% compared to the experimental data. Overall, the simulated residual velocities showed a good correlation with the experimental ones.

Table 5 Comparison of calculation results and experimental results.

Impact position	v_i/ (m s $^{-1}$)	v_r/ (m s $^{-1}$)		
		experiment	simulation	Relative error/%
Crown	828.4	718.8	636.7	-11.42
	604.2	509	492.0	-3.34
	427.7	345.6	339.7	-1.71
	294	219	204.9	-9.36
	214	115	103.9	-9.65
	166	—	—	—
Sidewall	454.2	388.8	383.6	-1.29
	209	155	141.7	-8.58
	144	—	—	—

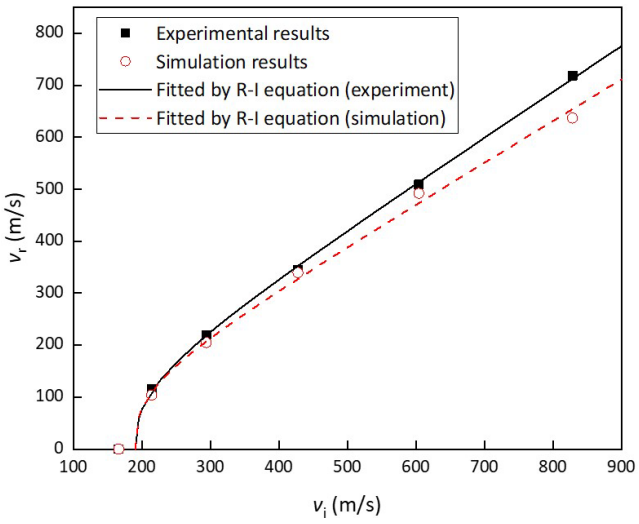

Figure 11 Fragment residual versus impact velocity curves.

3.3.2 Damage mode of the tire

Figure 12 presents a typical tire damage mode, where the front side is denoted by A, the back side by B, and the perforation is highlighted by a red circle. Since the rubber deformation at the entrance was completely elastic during the impact of the fragments, the edge of the perforation is smooth and concave, with an obvious circular deformation area. After the penetration of the fragment, the rubber around the entrance regains its shape under its own elasticity, leading to a smaller diameter of perforation at the entrance compared to the diameter of the fragment. In contrast, the edge of the perforation at exit is relatively rough, and its diameter is larger than the entrance. Moreover, due to the viscosity during the penetration process, the rubber adheres to the top of the fragments, leading to a small amount of material peeling off from the exit hole. Additionally, it can be observed that some steel cords in the tire were slightly exposed due to the penetration. Overall, the main failure mode of the tire includes local erosion in the center of the perforation, elastic deformation around the perforation, and tensile fracture of the steel cords.

Figure 13 presents a comparison of the tire perforation obtained from both the experiment and simulation conducted at an impact velocity of 427.7 m/s. The experiment and simulation yielded perforation diameters of about 2.6 mm and 3 mm, respectively, and the maximum crack lengths at the exit were approximately 9 mm and 8 mm,

respectively. The tire damage mode and perforation pattern obtained from the simulation were found to be consistent with the experimental results.

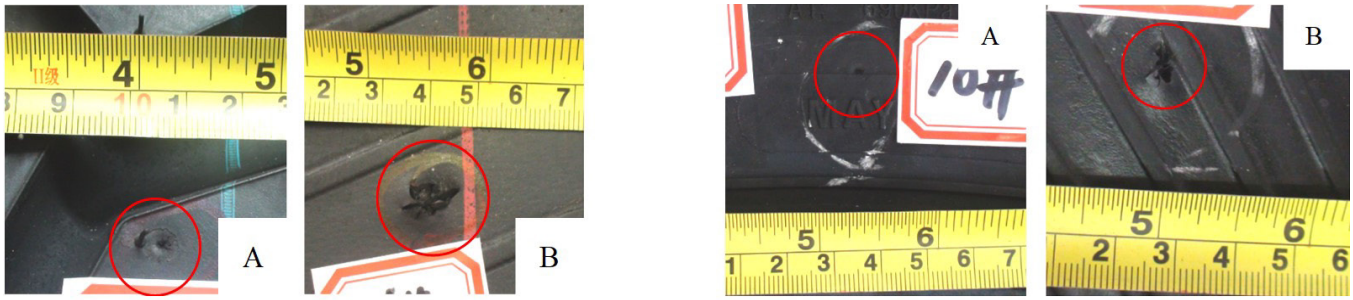

(a) v_i = 427.7 m/s. (b) v_i = 209 m/s.

Figure 12 Typical damage mode of the tire.

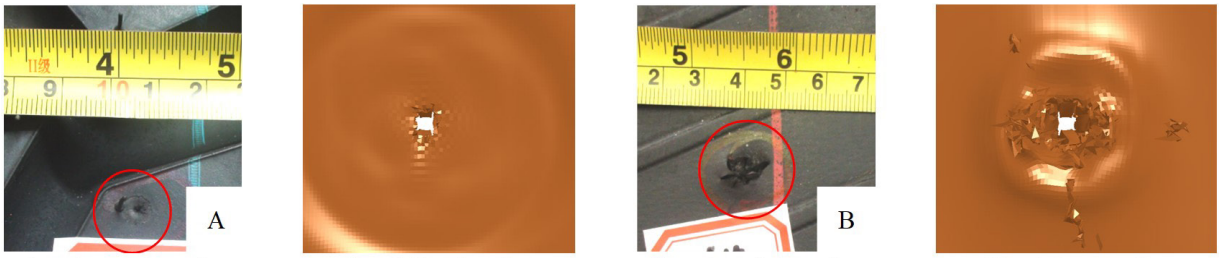

Experimental results. Simulation Results. Experimental results. Simulation results.

(a) entry. (b) exit.

Figure 13 Comparison of the perforation obtained by simulation and the experiment (v_i = 427.7 m/s)

4 RESULTS AND DISCUSSION

4.1 Penetration process

Figure 14 illustrates the process of the fragment penetrating the tire at a velocity of 427.7 m/s. To present the entire process more clearly, only half of the rubber is shown. Upon collision with the rubber, the high stress generated by the fragment causes a slight indentation at the entry point. Subsequently, the fragment compresses the rubber material during the penetration process, resulting in an accelerated radial motion. Due to the high elasticity of the rubber material, separation occurs between the rubber and the fragment. However, due to the radial velocity of the rubber, it continues to decelerate and expand, forming a cavity within the rubber. The size of the cavity reaches its maximum when the radial velocity of the rubber becomes zero, with a maximum diameter of approximately 14 mm (1.3 times the diameter of the fragment). After 70 μs, under the elastic behavior of the rubber material, the cavity gradually closes along the trajectory direction from the entry point, and its size decreases. Meanwhile, the fragment starts to come into contact with the cord fabric. The presence of the cord fabric constrains the deformation of the rubber, resulting in significantly smaller cavity sizes near the cord fabric compared to those near the entry point. The cord fabric experiences tension and fractures as a result of the fragment's penetration. After passing through the cord fabric, the fragment exits the tire after approximately 150 μs, carrying some peeled-off cord fabric. Due to the influence of the cord fabric and the boundary effects at the exit point, the shape of the cavity near the exit point differs from that near the entry point. As the rubber material along the path of the fragment penetration fails and is removed in the simulation, no distinct rubber plug is formed after the fragment penetration. At 170 μs, the cavity near the entry point is completely closed, with a size significantly smaller than that of the fragment. Throughout the entire process, the fragment undergoes rigid penetration without significant deformation.

Figure 15 shows the equivalent strain contour of rubber at different times. With the penetration of fragments, the high strain areas inside the rubber gradually expand outward and form a layered distribution. During the expansion and contraction stages of the cavity, the size of the plastic deformation zone around its surface increases. It can be inferred from the equivalent strain contour that the rubber mainly undergoes elastic deformation, and the maximum equivalent strain is always located at the position of the cavity wall and where the fragment directly contacts the rubber.

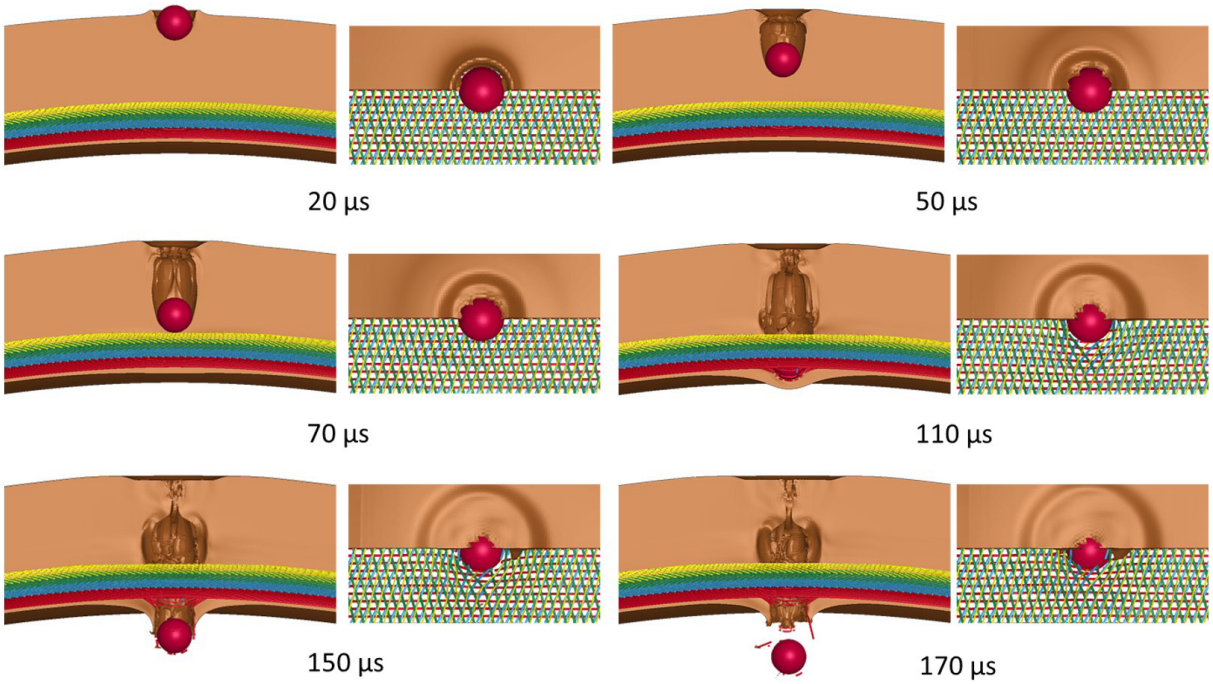

Figure 14 Penetration process of the fragment (left: side view, right: top view).

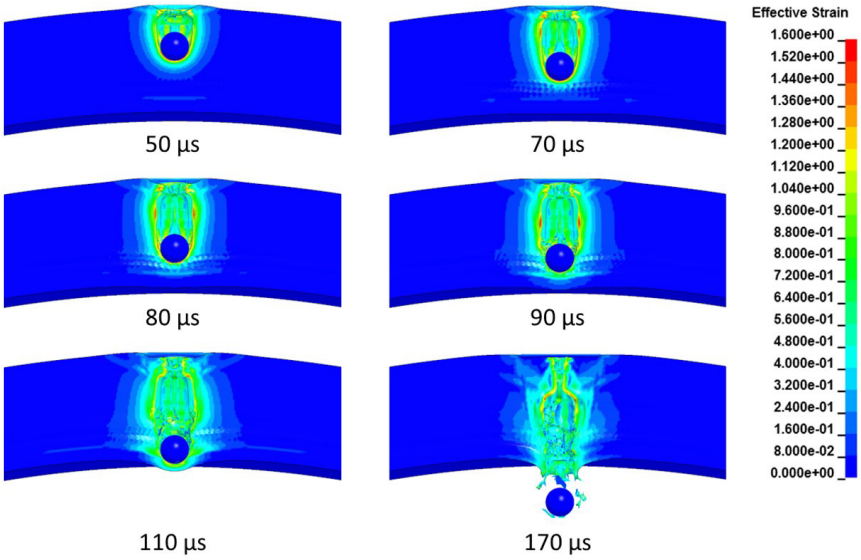

Figure 15 Effective strain contour of the rubber.

Figure 16 presents the variation of velocity and deceleration with time during the fragment penetration of the tire. Combining **Figure 14** to **Figure 16**, the process of fragment penetration can be divided into four stages:

1. Stage I (0 μs to 20 μs) represents the initial entry of the fragment, where the contact area between the fragment and the tire gradually increases. The deceleration of the fragment initially increases and then decreases.

2. Stage II (20 μs to 70 μs) corresponds to the stable penetration of the fragment into the rubber material, before direct contact with the cord fabric layer. During this stage, the deceleration of the fragment remains relatively constant, approximately half of the maximum deceleration observed during the first stage. This suggests that the resistance force exerted by the tire on the fragment remains nearly constant.

3. Stage III (70 μs to 105 μs) involves the interaction between the fragment and the cord fabric layer. The deceleration of the fragment increases again as it penetrates the cord fabric layer. As the cord fabric fractures, the deceleration decreases and reaches a value similar to that observed in Stage II after the fragment completely penetrates the cord fabric layer.

4. Stage IV (105 μs to fragment exits) represents the continued penetration of the fragment through the rubber material after passing the cord fabric layer. Due to the boundary effects, the deceleration of the fragment and the resistance it encounters gradually decrease until the fragment exits the tire.

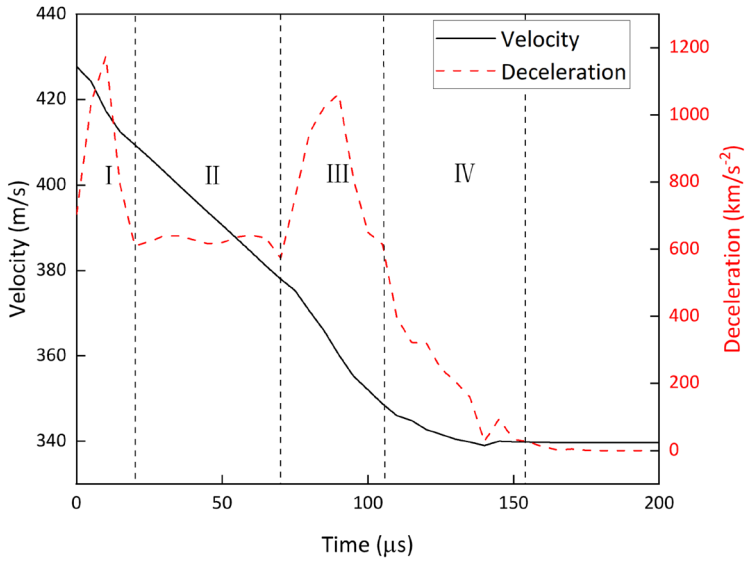

Figure 16 Motion curves of the fragment.

Figure 17 illustrates the changes in kinetic and internal energy of rubber and cord layers over time, it can be observed that the energy of the cord layer is two orders of magnitude smaller than that of the rubber layer, indicating that most of the energy lost by the fragment is absorbed by the rubber. The kinetic energy of fragments mainly transfers to the rubber in the form of cavity, and the kinetic energy of the rubber is primarily related to the velocity of cavity motion, while its internal energy is mainly determined by the volume of cavity. As revealed in **Figure 17**(a), the kinetic and internal energy of rubber increase rapidly during the first two stages; in Stage III, as the tail of the cavity begins to stop expanding and the cord's extension partially slows down the expansion of the cavity, the kinetic energy of rubber starts to decrease, but the internal energy of rubber continues to increase due to the continuous enlargement of cavity size. In the middle of Stage IV, due to the secondary expansion of cavity, part of internal energy of the cavity transforms into kinetic energy, causing a decrease in the internal energy of rubber and a secondary rebound in kinetic energy. It can be further inferred from **Figure 17**(b) that the kinetic energy of the four-layer cord reaches its maximum value in the order of contact with fragments, and then rapidly decreases as the cord is pulled apart. Since the fourth layer of cord has suffered pressure from fragment penetration before contact, although it contacts with the fragment last, its kinetic energy peak is the highest since. At the end of stage IV, i.e., after the fragment penetrates through the tire, the increase in kinetic energy of cavity due to cavity oscillation drives a partial rebound in the kinetic energy of the fourth layer of cord. The peak of internal energy of the cord increases in order of contact with fragments, and the time when it appears

is slightly delayed compared to that of kinetic energy. Once the peak internal energy of the cord is reached, its value no longer changes significantly.

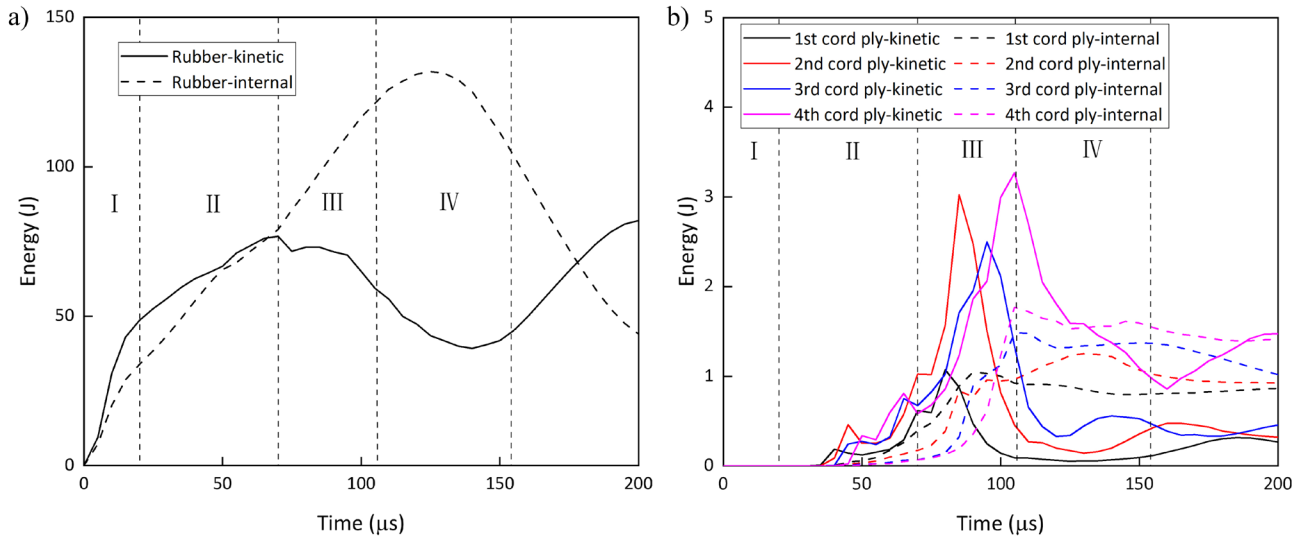

Figure 17 Energy change of rubber and cord ply.

Table 6 provides the kinetic energy consumption of the fragment in each stage. It can be observed that although Stage I has a relatively short duration, it accounts for approximately 20% of the total energy consumption throughout the process. The fragment consumes the most energy during Stages II and III, and the energy consumption in these two stages is roughly equivalent. This indicates that the penetration and energy dissipation of the fragment are significantly influenced by the cord fabric layer.

Table 6 The energy consumed in each stage of the process of fragment.

Stage	Energy consumption/J	Proportion/%
I	95.5	22.6
II	155.0	36.7
III	144.3	34.2
IV	27.1	6.4
Total	421.9	100

4.2 Parametric study

In addition to impact velocity, several factors can influence the dynamic response of the tire under the penetration of fragments, including obliquity, tire thickness, and fragment mass. This section aims to calculate and analyze the impact of these factors on the penetration ability of fragments.

4.2.1 Obliquity

Using the established numerical simulation model, calculations were performed for fragment penetration into tire crown and sidewalls at different obliquities ϑ. The obliquity ϑ is defined as the angle between the direction of fragment velocity and the outer normal of the surface at the impact point. The fragment velocities used in the simulations were

600 m/s and 400 m/s for crown penetration, and 400 m/s and 200 m/s for sidewall penetration. **Figure 18** illustrates the relationship between the impact velocity of fragments and the residual velocity. As can be seen, when the obliquity is in the range of 0° to 30°, the change of the obliquity has almost no effect on the residual velocity. When the obliquity is greater than 45°, residual velocity decreases rapidly with the increase of the obliquity, and the influence of the obliquity on the residual velocity increases significantly.

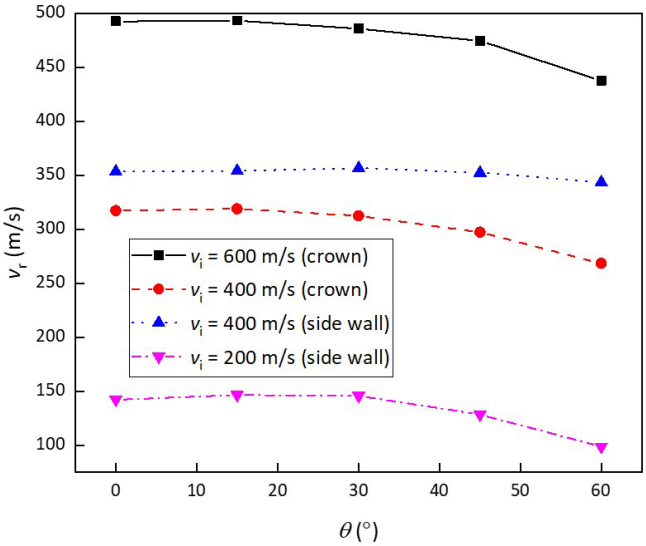

Figure 18 Effect of the obliquity on residual velocity.

Figure 19 shows the process of fragment penetration into the tire crown at different obliquities. The impact velocity of the fragments v_i in all cases is 400 m/s, and the red arrows in the figure represent the initial velocity direction of the fragments. To present the entire process more clearly, only half of the rubber and cord are shown. **Figure 20**(a) illustrates the variation in fragment velocity direction $\Delta\vartheta = \vartheta_1 - \vartheta$ for different obliquities. Here, ϑ_1 represents the angle between the velocity direction of the fragment during motion and the vertical direction. **Figure 20**(b) shows the deceleration variation of the fragments.

By analyzing **Figure 19** and **Figure 20**, it can be observed that during the entry stage (Stage I), $\Delta\vartheta$ is positive for oblique penetration. This indicates that the initial impact between the fragment and the tire slightly deflects the fragment's motion direction away from the vertical direction. Additionally, the deceleration (resistance) of the fragment decreases gradually with an increase in the obliquity. During the stable penetration stage (Stage II), $\Delta\vartheta$ vary differently for different obliquities. For ϑ = 15° and 30°, the fragment's motion direction continues to move away from the vertical direction. For ϑ = 45°, the fragment's motion direction remains relatively unchanged. However, for ϑ = 60°, $\Delta\vartheta$ gradually decreases and it becomes negative, indicating that the fragment's motion direction gradually approaches the vertical direction. Moreover, the rate at which $\Delta\vartheta$ decreases is faster than the rate at which $\Delta\vartheta$ increases when ϑ = 30°. The deceleration (resistance) of the fragment during oblique penetration does not differ significantly. However, due to the smaller contact area between the fragment and the rubber during oblique penetration compared to normal penetration, the deceleration (resistance) is lower during oblique penetration. During the cord layer penetration stage (Stage III), the asymmetric forces generated by the cords cause a slight increase in $\Delta\vartheta$. Additionally, as more cords participate in resisting the motion of the fragment during oblique penetration, the peak deceleration (resistance) of the fragment increases gradually with an increase in the obliquity. During the exit stage (Stage IV), the deceleration of the fragment gradually decreases due to the boundary effects of the back, and the asymmetric resistance caused by boundary effects causes the fragment's motion direction to progressively deviate from the vertical direction.

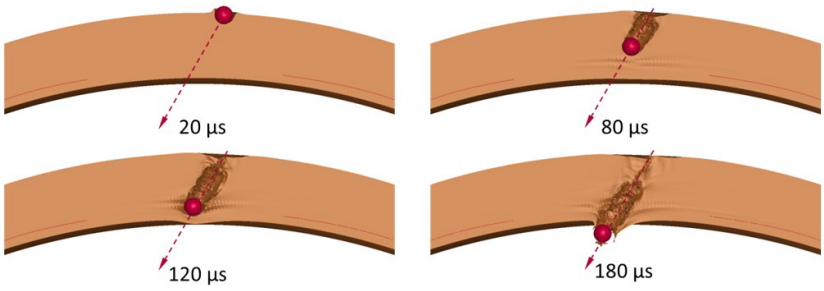

(b) ϑ = 30°.

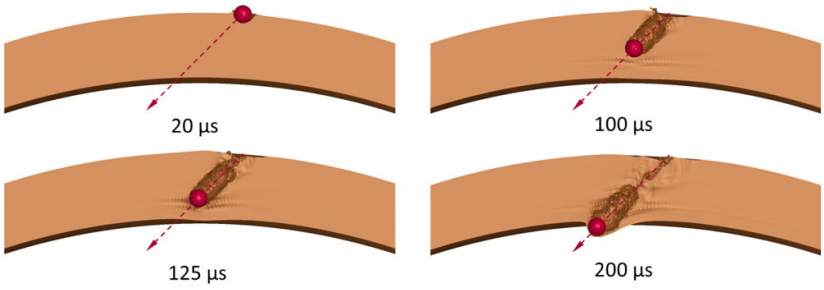

(c) ϑ = 45°.

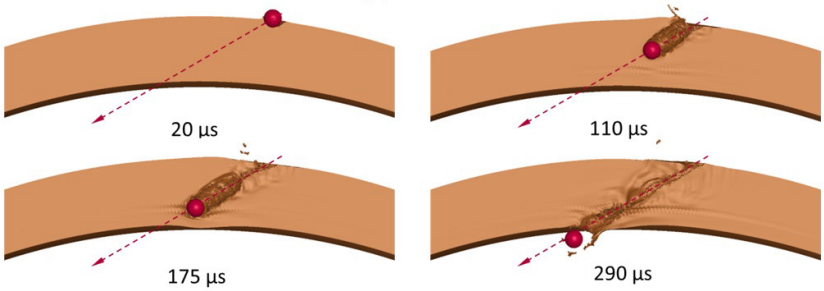

(d) ϑ = 60°.

Figure 19 The process of fragment penetrating the tire crown at different obliquities (v_i = 400 m/s).

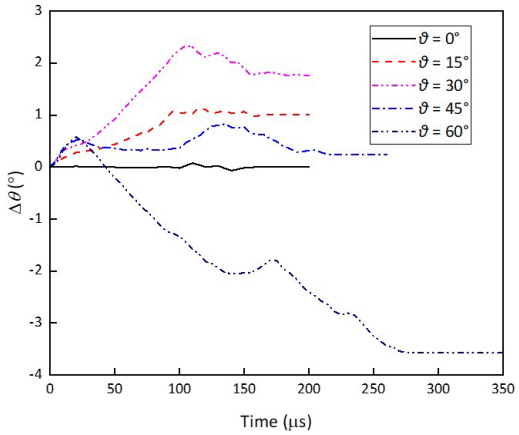

(a) $\Delta\vartheta$ versus time.

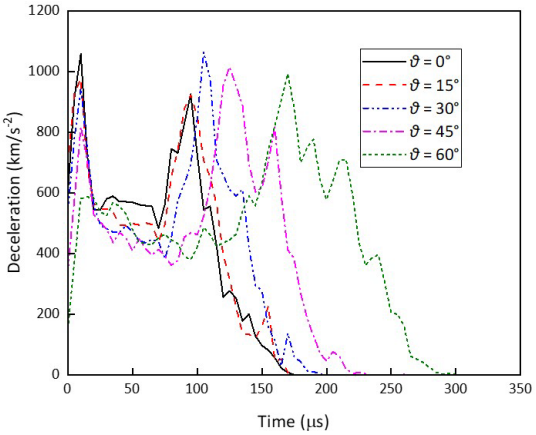

(b) deceleration versus time.

Figure 20. $\Delta\vartheta$ and deceleration of fragment versus time.

The ballistic limit velocity v_{bl} is an important quantity to measure the anti-penetration ability of the tire. **Figure 21** presents the ballistic limit velocity of the crown and sidewall of the tire at different obliquities. The results show that the limit velocity of fragments penetrating the tire crown vertically is 167.5m/s, while the limit velocity of penetrating the sidewall is 113.5 m /s. Moreover, the limit penetration velocity of the tire increases as the obliquity increases. Notably, the ballistic limit velocity of the crown is about 34% to 48% higher than that of the sidewall.

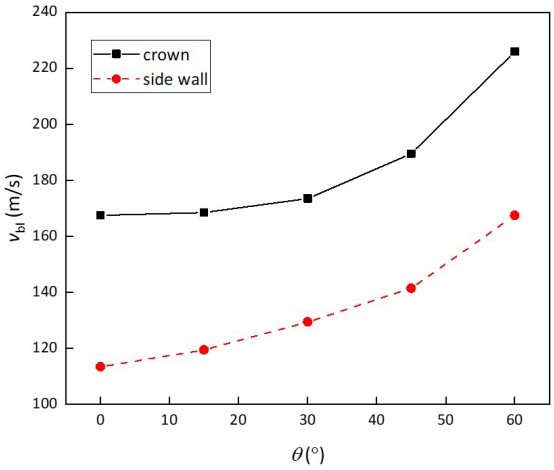

Figure 21 Ballistic limit velocities at different obliquities.

4.2.2 Tire thickness

The cord structures of the tire crown and sidewall exhibits notable differences. Additionally, the tire crown has two types of tread pattern with different thicknesses (*H*), while the sidewall thickness gradually increases from the center to the two sides. As a result, the variations in tire thickness were considerable over the tread and sidewall areas of the tires. Therefore, by changing the thickness of the rubber layer and hence the overall thickness of the tire, a numerical simulation model was established to investigate fragment penetration into tires of different thicknesses. **Figure 22** depicts the numerical simulation models of fragment penetration into tire crowns with thicknesses of 15mm and 35mm, which includes only one-quarter of the rubber layer and half of the cord to illustrate the model more clearly.

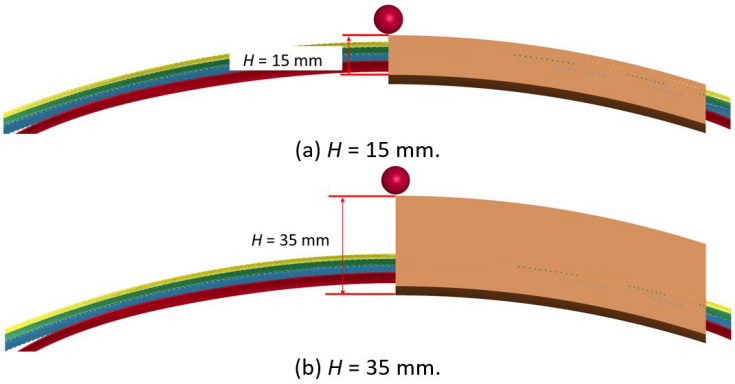

Figure 22 Typical models for fragment penetrating tire crown of different thicknesses.

Figure 23 shows the deceleration of fragment penetration into tire crowns of different thicknesses. It can be observed that, except for *H*=15mm, the deceleration patterns during the entry stage for the other thicknesses are consistent, and the peak deceleration values are essentially the same. However, at *H*=15mm, where the rubber thickness is relatively thin, the cord in the back of the rubber provides some support and reinforcement, resulting in a peak deceleration approximately 30% higher than that of the other thicknesses during this stage. After the fragment fully penetrates into the tire, a stable penetration stage corresponding to a plateau segment (**Figure 16**) is observed only in the deceleration curves corresponding to *H* ≥35mm. For the other thicknesses, the cord starts to influence the penetration of the fragment after it enters the rubber, so there is no clear observation of a distinct stable penetration stage. During the cord penetration stage, except for *H*=15mm, the deceleration patterns of the fragments for the other thicknesses are consistent. As the velocity of the

fragments upon contact with the cords decreases with increasing tire thickness, the resistance from the rubber and cords gradually diminishes, leading to a decrease in the peak deceleration as the tire thickness increases.

The ballistic limit velocity of fragments impacting different positions of the tire (with different thicknesses) was calculated and is presented in **Figure 24**. Since the tire crown possesses more cord layers than the sidewall, the ballistic limit velocity when fragments impact the tire crown is approximately 10% higher than that of the sidewall when the thickness is the same. This finding demonstrates that the cord structure enhances the anti-penetration ability of the tire.

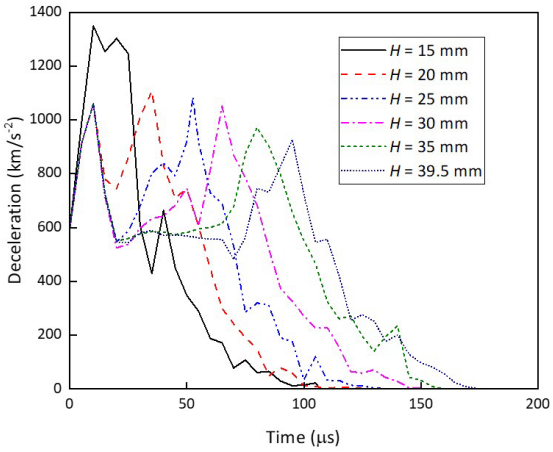

Figure 23 Deceleration of fragment versus time.

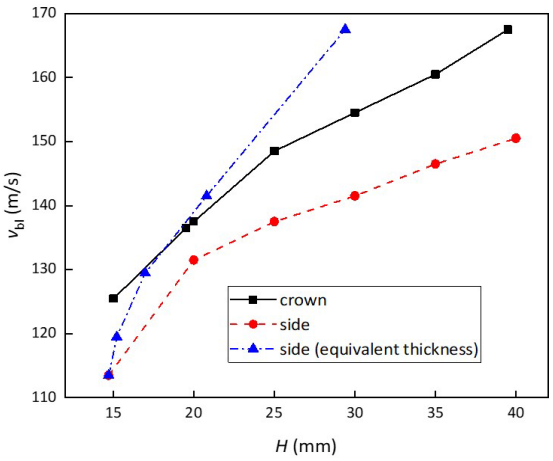

Figure 24 Ballistic limit velocities of different tire thickness.

Grote et al. (Grote et al., 1995) and Danish (Danish, 1968) both argue that the obliquity would not be a significant parameter for a "soft" target like tires except for the increase of the target line-of-sight thickness. According to section 4.2.1, it can be inferred that the angular deviation of the fragment during oblique penetration is relatively small. Therefore, the relationship between the equivalent thickness $H_{eq} = H \cdot \sec\vartheta$ corresponding to the same obliquity and the ballistic limit velocity in **Figure 21** was calculated when the fragments penetrated the tire sidewall at different obliquities. The results were then plotted in **Figure 24**. By comparing the critical velocities at which the fragments penetrate the tire sidewall under the two conditions, it can be observed that when the tire sidewall with a thickness H is penetrated obliquely at an angle ϑ, the fragments exhibit a higher ballistic limit velocity than when the thickness is H_{eq}.

We selected two cases from **Figure 24** where the actual thickness and equivalent thickness are similar: H = 20mm and H_{eq} = 20.8 mm (ϑ = 45°), and H = 30mm and H_{eq} = 29.4 mm (ϑ = 60°). A comparative analysis of the motion characteristics of the fragment was conducted, as shown in **Figure 25**. Based on **Figure 25** (a), it can be inferred that when the equivalent

thickness is the same, the velocity attenuation of the fragment during oblique penetration is slower, but its distance traveled inside the tire is longer, about 25% greater. Based on **Figure 25** (b), during the entry stage, the deceleration (resistance) of the fragment during oblique penetration is smaller than that during normal penetration with the same equivalent thickness. Additionally, during the stable penetration stage, the difference in deceleration (resistance) between the two conditions is not significant. During the cord penetration stage, the contact area and penetration path of the fragment with the cords are larger during oblique penetration, which results in a greater deceleration and resistance compared to normal penetration. As a result, the residual velocity of the fragment is lower during oblique penetration. Therefore, when the equivalent thickness is the same, the ballistic limit of the fragment into the tire during oblique penetration is higher. Simply calculating the penetration characteristics of the fragment in a tire during oblique penetration using an equivalent thickness that is the same as that for normal penetration with the same equivalent thickness is not accurate.

4.2.3 Fragment mass

The ballistic limit velocities of spherical tungsten fragments with different masses (m = 0.6 g, 2 g, 4 g, 6 g, 8 g, 10 g, 12.5 g) penetrates the tire normally were obtained, as shown in **Figure 26**. When the fragment mass was less than 4 g, the resistance of the tire decreases rapidly with the increase of the fragment mass. The ballistic limit velocity decreased approximately exponentially with the increase of fragment mass. When the fragment mass increased from 4 g to 12.5 g, the ballistic limit velocity of the crown and sidewall decreased by 19.5% and 23.1%, respectively.

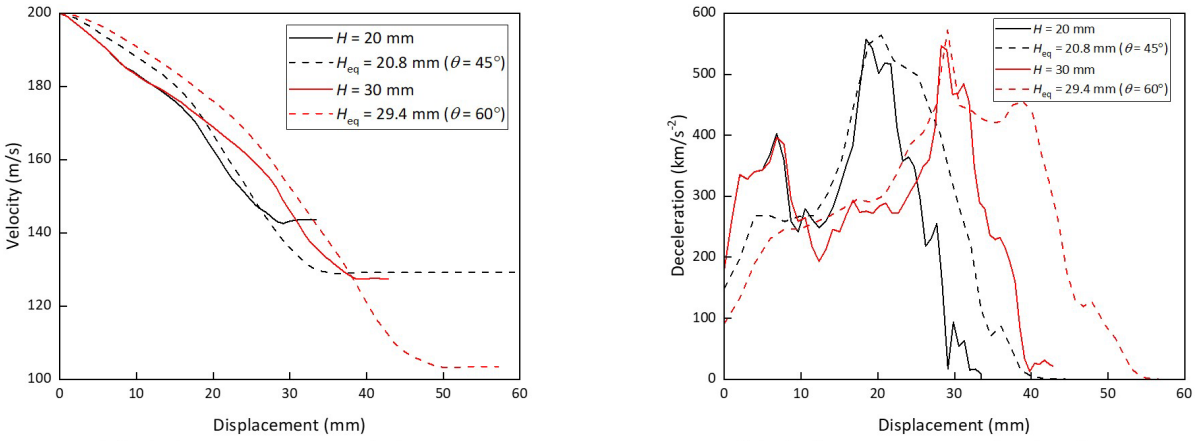

(a) Displacement versus velocity. (b) Displacement versus deceleration.

Figure 25 Comparison of the motion characteristics of the fragment

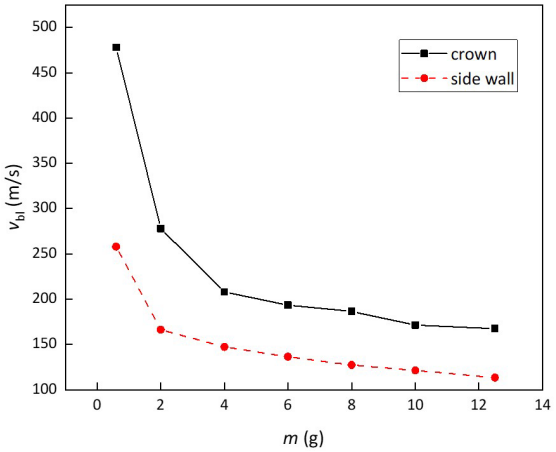

Figure 26 Ballistic limit velocity at different fragment masses.

4.3 Penetration equation

Following the form of THOR equation (Ballistic Analysis Laboratory et al., 1961), the following equation is used to fit the simulated ballistic limit:

$$v_{\mathrm{bl}} = a_1 H^{a_2} m^{a_3} \left(\cos\theta\right)^{a_4} \tag{5}$$

where a_1 to a_4 are fitted parameters. A least of square method is used to fitted the simulation results, the obtained parameters is shown in **Table 7**. As discussed in section 2.2, the cord structures of the tire crown and the sidewall are distinct, resulting in a higher ballistic limit velocity at the tire crown compared to the sidewall when the tire thickness is equivalent. Therefore, the fitted parameters are different for the crown and sidewall. **Figure 27** presents a comparison of the ballistic limit velocities obtained through calculations and simulations under different scenarios. The relative errors between the two are all less than 15%. Therefore, the fitted equation parameters can be utilized for subsequent vulnerability and damage assessment studies on military wheeled vehicles.

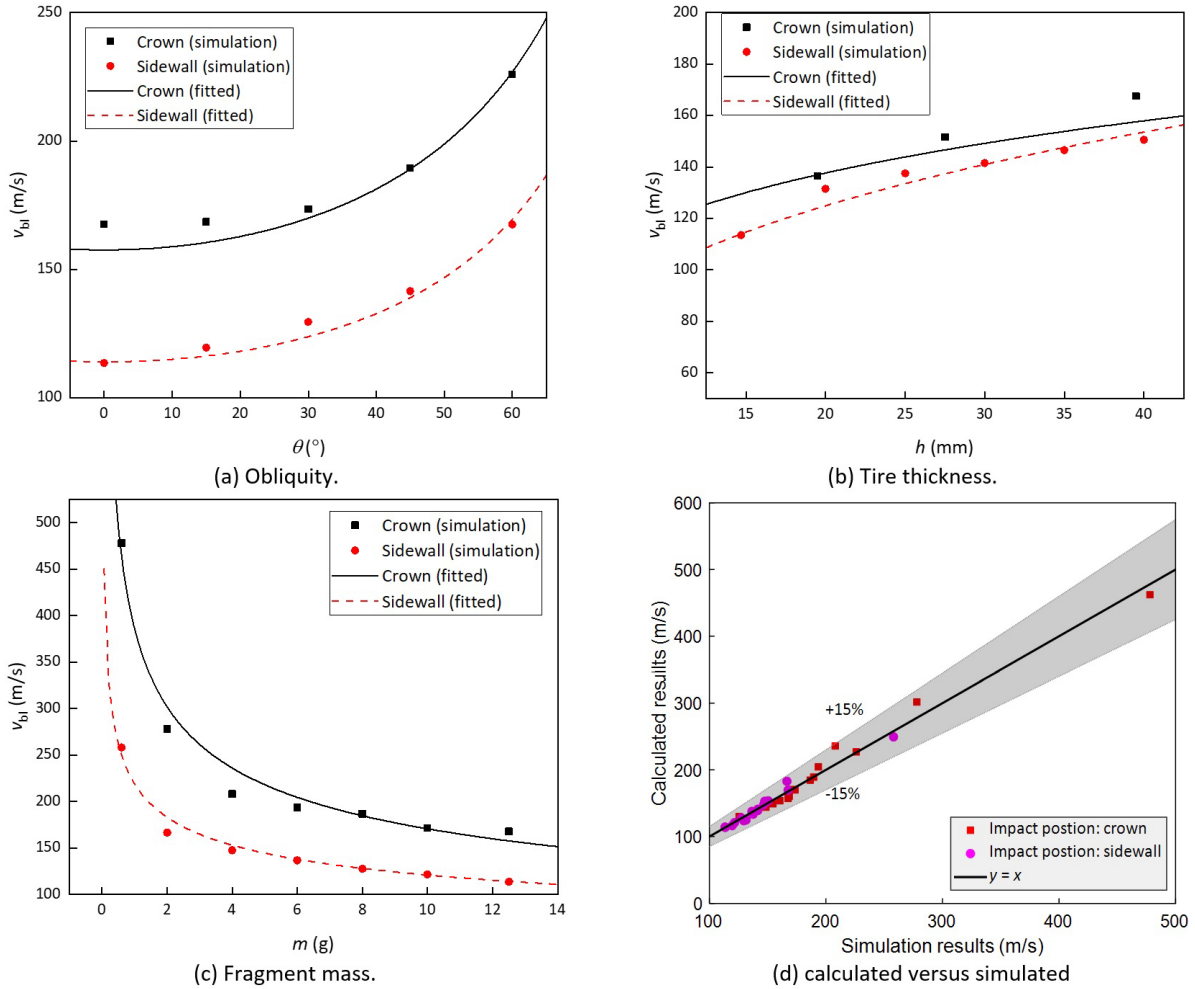

(a) Obliquity. (b) Tire thickness. (c) Fragment mass. (d) calculated versus simulated

Figure 27 Calculation and simulation results of ballistic limit.

Table 7 Fitted parameters.

Impact location	a_1	a_2	a_3	a_4
Crown	186.1	0.1982	-0.3544	-0.5265
Sidewall	98.2	0.2978	-0.2579	-0.5730

5 CONCLUSIONS

In the present study, experiments and simulation of fragments impacting tires of military vehicle were carried out. Results of the simulation were compared with experimental measurement of fragment residual velocity and tire damage mode; good agreements were obtained. The verified simulation model was further used to investigate several critical factors in fragment penetrating tires. The main conclusions of this work could be summarized as follows:

(1) The penetration of a fragment through a tire results in distinctive features at the entrance and exit points. Specifically, the edge of the entrance exhibits a smooth concave shape with a smaller diameter compared to that of the fragment, while the exit perforation displays a relatively rough edge and larger diameter than its entry counterpart. The main failure modes of the tire comprise local erosion near the center of the perforation, elastic deformation surrounding the perforation, and tensile fracture of the steel cords.

(2) The process of fragment penetration into a tire can be divided into four stages: the entry stage, stable penetration stage, cord layer penetration stage, and fragment exit stage. The cord structure demonstrates its ability to undergo plastic deformation to a certain extent and its restraining effect on the rubber material.

(3) When a fragment penetrates a tire obliquely, the change in its velocity direction, denoted as $\Delta\vartheta$, varies at different stages of penetration and is dependent on the obliquity. However, overall, $\Delta\vartheta$ is relatively small compared to the obliquity. When the equivalent thickness is the same, the ballistic limit of the fragment into the tire during oblique penetration is higher. Simply calculating the penetration characteristics of the fragment in a tire during oblique penetration using an equivalent thickness that is the same as that for normal penetration with the same equivalent thickness is not accurate.

(4) The empirical formula in the form of the Thor equation can accurately predict the ballistic limit velocity of fragments into different positions of the tire, with an error of less than 15%.

Author's Contributions: Conceptualization, Yangziyi Ji, Xiangdong Li; Methodology, Yangziyi Ji, Xiangdong Li and Lanwei Zhou; Investigation, Yangziyi Ji, Xingfeng Liu; Writing - original draft, Yangziyi Ji, Xingfeng Liu; Writing - review & editing, Yangziyi Ji, Xiangdong Li; Funding acquisition, Xiangdong Li; Resources, Xiangdong Li and Lanwei Zhou; Supervision, Xiangdong Li.

Editor: Marcílio Alves

References

Ballistic Analysis Laboratory, Institute for Cooperative Research, & The Johns Hopkins University. (1961). *The Resistance of Various Metallic Materials to Perforation by Steel Fragments; Empirical Relationships for Fragment Residual Velocity and Residual Weight*. Johns Hopkins Univ., Cockeysville, MD. Ballistic Analysis Lab.

Baranowski, P., Malachowski, J., Janiszewski, J., & Wekezer, J. (2016a). Detailed tyre FE modelling with multistage validation for dynamic analysis. *Materials & Design, 96*, 68–79. https://doi.org/ 10.1016/j.matdes.2016.02.029

Baranowski, P., Malachowski, J., & Mazurkiewicz, L. (2016b). Numerical and experimental testing of vehicle tyre under impulse loading conditions. *International Journal of Mechanical Sciences, 106*, 346–356. https://doi.org/10.1016/j.ijmecsci.2015.12.028

Baranowski, P., Małachowski, J., & Mazurkiewicz, Ł. (2019). Local blast wave interaction with tire structure. *Defence Technology*, S2214914719302533. https://doi.org/10.1016/j.dt.2019.07.021

Cai, L., Al-Ostaz, A., Li, X., & Fowler, C. (2016). Ballistic Resistance and Self-Sealing Behavior of Polyhedral Oligomeric Silsesquioxane (POSS)-Enhanced Hydrogenated Nitrile Butadiene Rubber (HNBR) Coating Under High Speed Impact. *International Journal of Advanced Materials Research, 2*(1), 1–12.

Cai, L., Al-Ostaz, A., Li, X., Fowler, C., Cheng, A. H.-D., & Alkhateb, H. (2015). Protection of steel railcar tank containing liquid chlorine from high speed impact by using polyhedral oligomeric silsesquioxane-enhanced polyurea. *International Journal of Impact Engineering, 75*, 1–10. https://doi.org/10.1016/j.ijimpeng.2014.06.015

Danish, M. B. (1968). *Perforation of Truck Tires by Compact Steel Fragments* (BRL-MR-1926). U.S. Army Ballistic Research Laboratory.

Danish, M. B. (1973). *Perforation of Radial Truck Tires by Compact Steel Fragments* (BRL-MR-2269). U.S. Army Ballistic Research Laboratory.

Grote, R. L., Moss, L. L., & Davisson, E. O. (1995). Penetration and Deflation Algorithms for Tire Vulnerability. *US Army Conference on Applied Statistics, 18-20 October 1995, 18*, 111.

Hall, W., Mottram, J. T., & Jones, R. P. (2004). Tire Modeling Methodology with the Explicit Finite Element Code LS-DYNA. *Tire Science and Technology, 32*(4), 236–261. https://doi.org/10.2346/1.2186783

Hallquist, J. O. (2007). LS-DYNA keyword user's manual. *Livermore Software Technology Corporation, 970*, 1–2.

Hong, D., Li, W., Zheng, Y., Jiang, N., & Pu, B. (2021). Process Analysis of Fragment Penetrating Natural Rubber Material. *Journal of Physics: Conference Series, 2002*(1), 012037. https://doi.org/10.1088/1742-6596/2002/1/012037

Ishikawa, N., Tanaka, N., Nishimoto, Y., & Ohno, T. (2005). *Impact behavior of hybrid rubber materials under rifle shooting*.

Khodadadi, A., Liaghat, G., Ahmadi, H., Bahramian, A. R., Anani, Y., Razmkhah, O., & Asemeni, S. (2019). Numerical and experimental study of impact on hyperelastic rubber panels. *Iranian Polymer Journal, 28*(2), 113–122. https://doi.org/10.1007/s13726-018-0682-x

Khodadadi, A., Liaghat, G., Taherzadeh-Fard, A., & Shahgholian-Ghahfarokhi, D. (2021). Impact characteristics of soft composites using shear thickening fluid and natural rubber–A review of current status. *Composite Structures, 271*, 114092. https://doi.org/10.1016/j.compstruct.2021.114092

Molnar, W., Nugent, S., Lindroos, M., Apostol, M., & Varga, M. (2015). Ballistic and numerical simulation of impacting goods on conveyor belt rubber. *Polymer Testing, 42*, 1–7. https://doi.org/10.1016/j.polymertesting.2014.12.001

Recht, R. F., & Ipson, T. W. (1963). Ballistic Perforation Dynamics. *Journal of Applied Mechanics, 30*(3), 384–390. https://doi.org/10/fgc56k

Sun, S., & Chen, W. (2021). Constitutive Modeling and Numerical Simulation of Rubber-Cord Composites. *Machinery Design & Manufacture, 03*, 53–56.

Zhang, Q., Shi, J., Suo, S., & Meng, G. (2020). Finite element analysis of rubber materials based on Mooney-Rivlin models and Yeoh models. *China Synthetic Ruubber Industry, 43*(06), 468–471.